

Microscopic three-cluster study of light exotic nuclei

P. Descouvemont*

Physique Nucléaire Théorique et Physique Mathématique, C.P. 229, Université Libre de Bruxelles (ULB), B 1050 Brussels, Belgium

(Received 6 February 2019; published 5 June 2019)

I develop a microscopic three-cluster model for exotic light nuclei. I use the hyperspherical formalism, associated with the generator coordinate method. This model is well adapted to halo nuclei, since the long-range part of the radial wave functions is accurately reproduced. The core wave functions are described in the shell model, including excited states. This technique provides large bases, expressed in terms of projected Slater determinants. Matrix elements involve seven-dimension integrals, and therefore require long calculation times. I apply the model to ^{11}Li , ^{14}Be , ^{15}B , and ^{17}N described by two neutrons surrounding a ^9Li , ^{12}Be , ^{13}B , and ^{15}N core, respectively. The ^{17}Ne (as $^{15}\text{O} + p + p$) and ^{15}Ne (as $^{13}\text{O} + p + p$) mirror nuclei are briefly discussed. I present the spectra and some spectroscopic properties, such as r.m.s. radii or $E2$ transition probabilities. I also analyze the importance of core excitations.

DOI: [10.1103/PhysRevC.99.064308](https://doi.org/10.1103/PhysRevC.99.064308)

I. INTRODUCTION

Exotic nuclei represent one of the major interests in modern nuclear physics [1]. These nuclei are located close to the driplines (neutron or proton) and, owing to the low binding energy, present specific properties, such as an anomalously large radius or modifications of the shell structure. Recent development of experimental facilities have provided a large number of new data, which need to be understood by theory.

The main property of exotic nuclei being their low binding energy, the relative wave functions extend to large distances. Theoretical models therefore need to reproduce this property. A widely used approach is the hyperspherical method [2], where the Jacobi coordinates are replaced by a set of angles, and by a single length, referred to as the hyperradius. The three-body equation is then replaced by a set of coupled differential equations depending on the hyperradius. The hyperspherical formalism can be extended to systems involving more than three particles [3]. Many works in atomic and in nuclear physics have been performed within this method.

In nuclear physics, most applications are carried out in non-microscopic models. In other words, the nucleus is seen as a three-body system, with a structureless core, and two external nucleons. Typical applications are the ^6He and ^{11}Li nuclei, modeled by $\alpha + n + n$ and $^9\text{Li} + n + n$ three-body structures. This approach therefore relies on nucleon + nucleon and nucleon + core potentials. It simulates the Pauli principle by an appropriate choice of these interactions. Core excitations are in general neglected.

This nonmicroscopic model can be extended to microscopic theories, where the system is described by a A -body Hamiltonian. The core nucleus is defined in the shell model, and a full antisymmetrization is taken into account. The use of the hyperspherical formalism guarantees the correct long-range behavior of the wave function. The model only relies

on a nucleon-nucleon interaction, and on the description of the core wave functions. In contrast with nonmicroscopic models, it allows me to include core excitations without any further parameter.

Microscopic cluster models are used in nuclear physics for many years (see reviews in Refs. [4,5]) but most applications deal with the two-cluster variant, much easier than multicluster approaches. The application of the hyperspherical formalism to microscopic cluster theories is recent. The first works were focused on ^6He [6,7], which involves the α particle as a core. The α particle can be accurately described by a $(0s)^4$ shell-model configuration, which makes the calculations relatively easy. The model was extended to three-body continuum states [8], and microscopic ^6He wave functions have been used in CDCC calculations of elastic scattering on heavy targets [9].

The main limitation of microscopic three-cluster models in hyperspherical coordinates is that the matrix elements involve the numerical calculation of (many) seven-dimension integrals [7]. Consequently, applications are essentially limited to light systems, most of them involving an α core. In addition to the ^6He system mentioned above, a recent application focuses on ^8Li , described by an $\alpha + ^3\text{H} + n$ three-cluster configuration [10].

The aim of the present work is to go beyond this limitation. The development of the computing technology, and in particular of the parallelization possibilities permits to consider heavier systems, involving p -shell nuclei as the core. I analyze four nuclei (^{11}Li , ^{14}Be , ^{15}B , ^{17}N) which are modelled by a p -shell core and two surrounding neutrons. Compared to previous applications, the present calculations face two difficulties: (i) the presence of p -shell orbitals, and (ii) the need of several Slater determinants for the core.

The paper is organized as follows. In Sec. II, I present a general overview of the microscopic three-cluster model. In Sec. III, I apply the method to various exotic nuclei. Concluding remarks are presented in Sec. IV.

*pdesc@ulb.ac.be

II. MICROSCOPIC THREE-CLUSTER MODEL IN HYPERSPHERICAL COORDINATES

A. General overview

My main goal is to solve a A -body problem, where the Hamiltonian is given by

$$H = \sum_{i=1}^A t_i + \sum_{i<j=1}^A v_{ij}. \quad (1)$$

In this definition, t_i is the kinetic energy of nucleon i , and v_{ij} a nucleon-nucleon interaction, which contains nuclear and Coulomb components. Recent *ab initio* models (see, for example, Ref. [11]) are developed to find exact solutions of the Schrödinger equation associated with (1). These models, however, are in general not well adapted to halo nuclei, where the long-range part of the wave functions plays a crucial role. My approach, in contrast, is based on the cluster approximation [4,12].

The total wave function, solution of the Schrödinger equation

$$(H - E)\Psi = 0, \quad (2)$$

is written schematically as

$$\Psi = \mathcal{A}\phi_1\phi_2\phi_3G, \quad (3)$$

where ϕ_i are the internal wave functions of the clusters (in practice, they are defined in the shell model), and G is a radial function, depending on the relative coordinates between the clusters. The antisymmetrization operator \mathcal{A} ensures that the wave function is completely antisymmetric.

The cluster approximation permits a strong simplification of the calculations, in comparison with *ab initio* models. It is also well adapted to halo nuclei or, more generally, to states presenting a strong cluster structure. Owing to this approximation, however, effective nucleon-nucleon interactions v_{ij} , such as the Volkov [13] or the Minnesota [14] force, must be used. These forces simulate missing effects, such as the tensor component, by an effective central interaction. Ideally, three-body forces should be introduced, and developments have been achieved in that direction for realistic forces (see Ref. [15] for a review). For effective interactions, however, even if some work has been done [16,17], the use of three-body forces is essentially limited to well bound nuclei, such as ^{12}C or ^{16}O . In most cluster calculations, three-body forces are therefore neglected.

Several variants of microscopic cluster models exist. Of course, the simplest version is a two-cluster model, which has been used for many years [18]. Three-cluster models have been developed in various directions: frozen triangular configurations [19], $2 + 1$ configurations essentially aimed for nucleus-nucleus scattering such as $^7\text{Be} + p$ [20], and, more recently, genuine three-body models using the hyperspherical formalism [7]. The present work is based on the hyperspherical approach, which is described in more detail in the next sections.

B. Core wave functions

Let me consider Eq. (3) where the internal wave functions ϕ_i are associated with three clusters with nucleon numbers (A_1, A_2, A_3) and charge numbers (Z_1, Z_2, Z_3) . I assume that clusters 2 and 3 are s -shell nuclei and, more specifically in the present work, that they are neutrons. I also assume that the oscillator parameter b is common to the three clusters. Until now, the use of the hyperspherical formalism in microscopic models was limited to an α core. This is well adapted, for example, to ^6He [7], ^6Li [7], or ^8B [10]. The main reason for this limitation is that, as it will be discussed later, matrix elements involve seven-dimensional integrals.

This limitation, however, restricts the applications to a few light nuclei. In the present work, I go beyond this limitation, and extend the model to p -wave orbitals. The consequences in terms of computer times are twofold: (i) the matrix elements involve p -shell orbitals, which has a strong impact on the matrix elements of the nucleon-nucleon interaction (quadruple sums over the individual orbitals); (ii) p -shell nuclei such as ^9Li or ^{12}Be involve several Slater determinants (up to 90 for ^9Li), whereas the α particle is described by a single Slater determinant.

I remind here the main properties. Let me consider a Slater determinant $\bar{\Phi}_i$ involving A_1 single-particle orbitals

$$\varphi_{n_x n_y n_z m_s m_t}(\mathbf{r}) = \varphi_{n_x}(x)\varphi_{n_y}(y)\varphi_{n_z}(z) \left| \frac{1}{2}m_s \right| \left| \frac{1}{2}m_t \right\rangle, \quad (4)$$

where $\varphi_n(s)$ are harmonic oscillator functions and where $m_s, m_t = \pm 1/2$ are associated with the spin and the isospin, respectively. The first step is to define the list of N_S Slater determinants consistent with the Pauli principle. Assuming that the s shell is filled, the number of Slater determinants for p -shell nuclei is $N_S = C_6^{Z_1-2} \times C_6^{N_1-2}$, where C_i^j is the number of combinations of j elements among i elements. For ^9Li , ^{12}Be , ^{13}B , and ^{15}N , I have $N_S = 90, 15, 20, 6$, respectively. The N_S Slater determinants $\bar{\Phi}_i$ must be projected on the various angular momenta I, L, S, T from a diagonalization of the I^2, L^2, S^2 , and T^2 operators ($I = L + S$). This procedure provides basis functions with good quantum numbers as

$$\Phi_{1,LST}^{I\nu} = \sum_{i=1}^{N_S} d_i^{I\nu LST} \bar{\Phi}_i. \quad (5)$$

Finally, basis functions (5) are used to diagonalize the Hamiltonian (1) for cluster 1, and I get the core wave functions as

$$\Phi_1^{I\nu} = \sum_{LST} D_{LST}^{I\nu} \Phi_{1,LST}^{I\nu}. \quad (6)$$

This technique corresponds to a standard shell-model approach, and can be extended to higher shells (the summation may involve an additional quantum number, associated with the degeneracy). The specificity of the cluster model is that (6) is only the very first step of the calculations. These internal wave functions must then be introduced in the three-body wave functions (3).

C. Three-cluster wave functions

Let me come back to the three-cluster wave functions (3). In the generator coordinate method (GCM, see Refs. [4,18]),

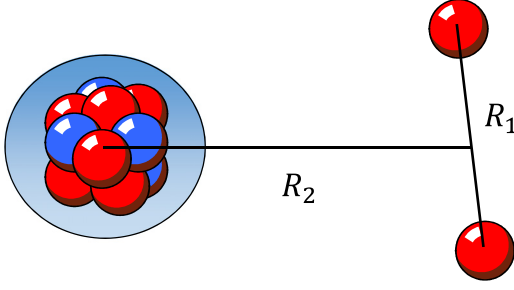


FIG. 1. Three-cluster configuration using the generator coordinates \mathbf{R}_1 and \mathbf{R}_2 [see Eq. (7)].

the clusters are located at three points, as represented in Fig. 1. The generator coordinates \mathbf{R}_1 is associated with the external clusters (neutrons in the present applications) and \mathbf{R}_2 with the relative motion between the core and the c.m. of clusters 2 and 3. They are variational parameters, and are not associated with the nucleon coordinates (in other words, the antisymmetrization operator does not act on \mathbf{R}_1 and \mathbf{R}_2). A GCM basis state is defined as

$$\begin{aligned} \Phi_{c_1}^{\nu_1\nu_2\nu_3}(\mathbf{R}_1, \mathbf{R}_2) = & \mathcal{A}\Phi_{c_1}^{\nu_1}\left(-\frac{A_{23}}{A}\mathbf{R}_2\right)\Phi_2^{\nu_2}\left(\frac{A_{23}}{A}\mathbf{R}_2 + \frac{A_1}{A_{12}}\mathbf{R}_1\right) \\ & \times \Phi_3^{\nu_3}\left(\frac{A_{23}}{A}\mathbf{R}_2 - \frac{A_1}{A_{12}}\mathbf{R}_1\right), \end{aligned} \quad (7)$$

where $\Phi_{c_1}^{\nu_1}$ are the core wave functions (6), and $\Phi_2^{\nu_2}$ and $\Phi_3^{\nu_3}$ correspond to the external clusters. In this equation, $A_{12} = A_1 + A_2$ and $A_{23} = A_2 + A_3$. If the internal wave functions are defined in the harmonic oscillator model with a common oscillator parameter b , these basis functions are Slater determinants, and the c.m. motion is factorized exactly. For the sake of clarity, I do not write the spins I_i of the clusters.

A first angular-momentum coupling is performed on the spins I_2 and I_3 of the external clusters with

$$\begin{aligned} \Phi_{c_1}^{I_2 I_3 I \nu}(\mathbf{R}_1, \mathbf{R}_2) = & \sum_{\nu_1 \nu_2 \nu_3} \langle I_2 \nu_2 I_3 \nu_3 | I \nu \rangle \Phi_{c_1}^{\nu_1 \nu_2 \nu_3}(\mathbf{R}_1, \mathbf{R}_2). \end{aligned} \quad (8)$$

Then I introduce the hyperspherical formalism, well known in nonmicroscopic models [21], and extended more recently to microscopic theories [7,22]. I define scaled Jacobi coordinates as

$$\mathbf{X} = \sqrt{\frac{A_2 A_3}{A_{23}}}\mathbf{R}_1, \quad \mathbf{Y} = \sqrt{\frac{A_1 A_{23}}{A}}\mathbf{R}_2, \quad (9)$$

which provide the hyperradius R and hyperangle α from

$$R = \sqrt{\mathbf{X}^2 + \mathbf{Y}^2}, \quad \tan \alpha = Y/X. \quad (10)$$

Both coordinates are complemented by the angles associated with \mathbf{X} and \mathbf{Y} as

$$\Omega_5 = (\alpha, \Omega_X, \Omega_Y). \quad (11)$$

From the basis functions (8), I project on the total angular momentum J and parity π . This is achieved by a double

projection on the orbital momenta ℓ_x and ℓ_y ; a projected basis function is written as

$$\begin{aligned} \tilde{\Phi}_{c_1 I_2 I_3 I \ell_x \ell_y L}^{JM\pi}(\mathbf{R}_1, \mathbf{R}_2) \\ = \sum_{\nu M_L} \langle I \nu L M_L | J M \rangle \int d\Omega_X d\Omega_Y \\ \times [Y_{\ell_x}^*(\Omega_X) \otimes Y_{\ell_y}^*(\Omega_Y)]^{LM_L} \Phi_{c_1}^{I_2 I_3 I \nu}(\mathbf{R}_1, \mathbf{R}_2), \end{aligned} \quad (12)$$

which represents a four-dimension integral. This double-projection technique has been used in three-body models aimed at studying nucleus-nucleus scattering such as ${}^7\text{Be} + p$ [23] for example. In the hyperspherical formalism, one introduces the hypermoment K , which is a generalization of the angular momentum in three-body systems. An hyperspherical basis function reads

$$\begin{aligned} \Phi_{\gamma K}^{JM\pi}(R) = & \int d\alpha \cos^2 \alpha \sin^2 \alpha \varphi_K^{\ell_x \ell_y}(\alpha) \\ & \times \tilde{\Phi}_{\gamma}^{JM\pi}(R \sin \alpha, R \cos \alpha), \end{aligned} \quad (13)$$

where index γ stands for $\gamma = (c_1 I_2 I_3 I \ell_x \ell_y L)$. In this equation, function $\varphi_K^{\ell_x \ell_y}(\alpha)$ is defined by

$$\begin{aligned} \varphi_K^{\ell_x \ell_y}(\alpha) = & \mathcal{N}_K^{\ell_x \ell_y} (\cos \alpha)_R^{\ell_y} (\sin \alpha)_R^{\ell_x} \\ & \times P_n^{\ell_y + 1/2, \ell_x + 1/2}(\cos 2\alpha), \end{aligned} \quad (14)$$

$P_n^{a,b}(x)$ being a Jacobi polynomial. The normalization coefficient $\mathcal{N}_K^{\ell_x \ell_y}$ is given by

$$\mathcal{N}_K^{\ell_x \ell_y} = \left[\frac{2n!(K+2)(n+\ell_x+\ell_y+1)!}{\Gamma(n+\ell_x+\frac{3}{2})\Gamma(n+\ell_y+\frac{3}{2})} \right]^{\frac{1}{2}}, \quad (15)$$

where $n = (K - \ell_x - \ell_y)/2$ is a positive integer. The main advantage of the hyperspherical formalism is to reduce the number of degrees of freedom to one. The configuration space is therefore spanned by a single generator coordinate R . This approach is also well adapted to three-body continuum states [8]. Of course, matrix elements between basis states (13) are more demanding in terms of computer times, since they involve seven-dimensional integrals (see next subsection), which must be performed numerically.

The total wave function of the system is given by a superposition of basis functions (13) as

$$\Psi^{JM\pi} = \sum_{\gamma K} \sum_{i=1}^N f_{\gamma K i}^{J\pi} \Phi_{\gamma K}^{JM\pi}(R_i), \quad (16)$$

where N is the number of generator coordinates (typically $N \approx 10$). In this expansion, the summation over the hypermoment K is limited to a maximum value K_{\max} . As usual in hyperspherical models, K_{\max} must be large enough to ensure the convergence of the physical quantities (energies, radii, etc.). Coefficients $f_{\gamma K i}^{J\pi}$ represent the generator function, and are obtained from a diagonalization of the Hamiltonian kernel.

D. Matrix elements

The main part of the calculation concerns matrix elements between projected basis functions (13). The Hamiltonian kernel reads

$$\begin{aligned} H_{\gamma K, \gamma' K'}^{J\pi}(R, R') &= \langle \Phi_{\gamma K}^{J\pi}(R) | H | \Phi_{\gamma' K'}^{J\pi}(R') \rangle \\ &= \int \cos^2 \alpha \sin^2 \alpha \cos^2 \alpha' \sin^2 \alpha' \varphi_K^{\ell_x \ell_y}(\alpha) \varphi_{K'}^{\ell_x \ell_y}(\alpha') \tilde{H}_{\gamma, \gamma'}^J(R \sin \alpha, R \cos \alpha; R' \sin \alpha', R' \cos \alpha') d\alpha d\alpha', \end{aligned} \quad (17)$$

where

$$\tilde{H}_{\gamma, \gamma'}^J(R_1, R_2; R'_1, R'_2) = \langle \tilde{\Phi}_{\gamma}^{J\pi}(R_1, R_2) | H | \tilde{\Phi}_{\gamma'}^{J\pi}(R'_1, R'_2) \rangle, \quad (18)$$

with $\tilde{\Phi}_{\gamma}^{J\pi}(R_1, R_2)$ given by Eq. (12). The projection over the hypermoment therefore represents a double integration over α and α' . This quadrature is performed numerically. From Eq. (12), the matrix elements (18) involve eight angular integrals. In fact, owing to the rotation invariance, three angles can be fixed, which leads to five-dimensional integrals. The calculation provides

$$\begin{aligned} \langle \tilde{\Phi}_{\gamma}^{J\pi}(R_1, R_2) | H | \tilde{\Phi}_{\gamma'}^{J\pi}(R'_1, R'_2) \rangle &= \frac{8\pi^2}{2J+1} \sum_{M_L, M'_L, \nu, \nu'} \langle I \nu L M_L | J \nu + M_L \rangle \langle I' \nu' L' M'_L | J \nu' + M'_L \rangle \\ &\times \int [Y_{\ell_x}^*(\Omega_{X'}) \otimes Y_{\ell_y}^*(0, 0)]^{L M_L} [Y_{\ell_x}(\Omega_{X'}) \otimes Y_{\ell_y}(\theta_{Y'}, 0)]^{L' M'_L} \\ &\times \langle \Phi_{c_1}^{I_{23} J \nu}(R_1, R_2) | H | \Phi_{c'_1}^{I'_{23} J \nu'}(R'_1, R'_2) \rangle d\Omega_X d\Omega_{X'} \sin \theta_{Y'} d\theta_{Y'}, \end{aligned} \quad (19)$$

where \mathbf{R}_2 is along the z axis and \mathbf{R}'_2 is in the xz plane. This expression is also valid for other rotation-invariant operators. A generalization to operators, such as the electromagnetic operators, is straightforward.

The calculation of the matrix elements (18) is therefore performed in several steps:

- (i) Matrix elements between Slater determinants $\mathcal{A}\tilde{\Phi}_1\Phi_2^{\nu_2}\Phi_3^{\nu_3}$ are first computed. One-body operators involve double sums over the individual orbitals, whereas two-body operators involve quadruple sums. When dealing with three s clusters, the quadruple sums contain 3^4 terms, but this amounts to 6^4 when one cluster belongs to the p shell. Compared to previous works on ${}^6\text{He}$ or ${}^{12}\text{C}$ this property makes the calculations 16 times longer.
- (ii) Matrix elements between wave functions (7) are then constructed with the transformation coefficients (6). The number of three-cluster Slater determinants is given by $N_S(2I_2 + 1)(2I_3 + 1)$. For ${}^6\text{He}$, this number is 4, since the core is an α particle. For ${}^{11}\text{Li}$, in contrast, the core involves 90 functions, and the total number of Slater determinants (7) is therefore 360.
- (iii) The next step is to compute the projected matrix elements (19), which involve five numerical quadratures (typically ≈ 16 – 20 points are used for each angle).
- (iv) Finally the projection over the hypermomentum is performed with (17). For a given set of generator coordinates (R, R') , all integrals are evaluated simultaneously.

This process must be repeated for all sets of (R, R') values. For systems such as ${}^{11}\text{Li}$, which involve many Slater determinants, the full calculation is extremely time consuming. This

can be achieved with an optimization of the codes, and using modern computing facilities. In practice, a parallelization is performed over the hyperangles α and α' in Eq. (17). Let me also mention that the total number of basis functions (i.e., the size of the matrices) can be as large as 20000. This raises precision issues since the basis is (highly) nonorthogonal.

III. APPLICATION TO LIGHT EXOTIC NUCLEI

A. Conditions of the calculations

The calculations are performed with the Volkov V2 nucleon-nucleon interaction [13]. For the oscillator parameter, I use $b = 1.60$ fm, a standard value for p -shell nuclei. The optimal b value stems from a compromise: to reproduce the core radius, and to minimize the binding energy of the core. Small variations of b can be compensated by a slight readjustment of the nucleon-nucleon interaction. The first step is to determine the core wave functions (6), as mentioned in Sec. II B. Including all p -shell configurations provides (90, 15, 20, 6) Slater determinants $\tilde{\Phi}_i$ [see Eq. (5)] for ${}^9\text{Li}$, ${}^{12}\text{Be}$, ${}^{13}\text{B}$, and ${}^{15}\text{N}$, respectively. The possible quantum numbers (I, L, S, T) are discussed in the Appendix. For ${}^9\text{Li}$, which has a $I = 3/2^-$ ground state, I limit the states to $I = 1/2, 3/2$, and to $T = 3/2$ to keep the size of the basis within acceptable values.

Values of the generator coordinate R are selected from 1.5 to 15 fm with a step of 1.5 fm. For the maximum hypermomentum, I use $K_{\max} = 16$. These conditions are sufficient to ensure the convergence of the energies and r.m.s. radii.

The central V2 interaction is complemented by a zero-range spin-orbit force with amplitude S_0 [7]. This amplitude is fixed to 40 MeV fm^5 , except for ${}^{11}\text{Li}$, where I use $S_0 = 50 \text{ MeV fm}^5$. The Volkov potential contains the admixture parameter M , whose standard value is $M = 0.6$. This value,

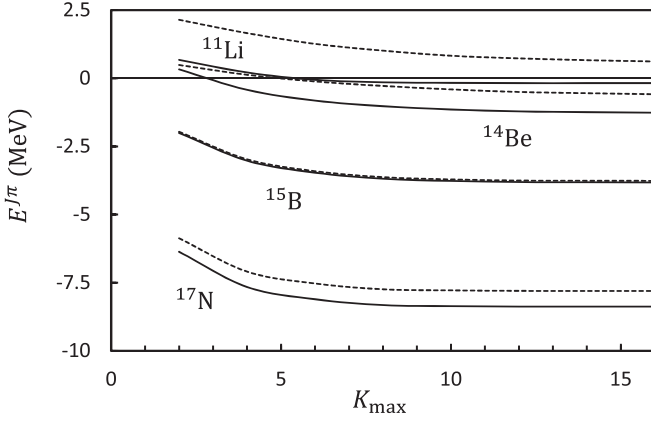


FIG. 2. Ground-state energies (with respect to the core + $n + n$ threshold) as a function of the maximum hypermomentum K_{\max} . The dotted lines are obtained by neglecting core excitations.

however, can be slightly modified without changing the fundamental properties of the interaction. The aim is to reproduce exactly the ground-state energies. For weakly bound nuclei, the properties are sensitive to the long-range part of the wave function, and therefore to the binding energies. With $M = 0.7750, 0.6119, 0.5945$, and 0.6177 , I reproduce the experimental two-neutron separation energies S_{2n} of ^{11}Li , ^{14}Be , ^{15}B , and of ^{17}N , respectively (0.370 MeV, 1.27 MeV, 3.75 MeV, and 8.37 MeV [24]).

In Fig. 2, I present the convergence of the ground-state energies with the maximum hypermomentum K_{\max} . In all cases, $K_{\max} = 16$ guarantees a good convergence. In this general overview, I also evaluate the importance of core excitations. In Fig. 2, the dotted lines represent the energies obtained by neglecting core excitations. This is done in Eq. (20) by keeping only γ values corresponding to the ground state of the core. In ^{14}Be and in ^{15}B , this effect is of the order of 0.6 MeV. It is quite small in ^{17}N : core excitations are negligible in the ground state. For ^{11}Li , the ground state is unbound if core excitations are neglected. The energy difference is of the order of 0.9 MeV.

I discuss now the properties of each nucleus by increasing mass, except for ^{11}Li , which I present as last application since, by far, it is the most complicated.

B. ^{14}Be as a $^{12}\text{Be} + n + n$ system

Before considering a full diagonalization of the basis, I first display the energy curves, where a single value of the generator coordinate R is considered. The energy curves $E_i^{J\pi}(R)$ are therefore obtained from the eigenvalue problem

$$\sum_{K'\gamma'} [H_{\gamma K, \gamma' K'}^{J\pi}(R, R) - E_i^{J\pi}(R) N_{\gamma K, \gamma' K'}^{J\pi}(R, R)] f_{\gamma' K'}^{J\pi} = 0, \quad (20)$$

where $N_{\gamma K, \gamma' K'}^{J\pi}(R, R')$ is the overlap kernel. They provide a useful overview of the system. From the attractive or repulsive character, one can predict the existence of bound states (or of narrow resonances). In all cases, the three-body threshold is subtracted.

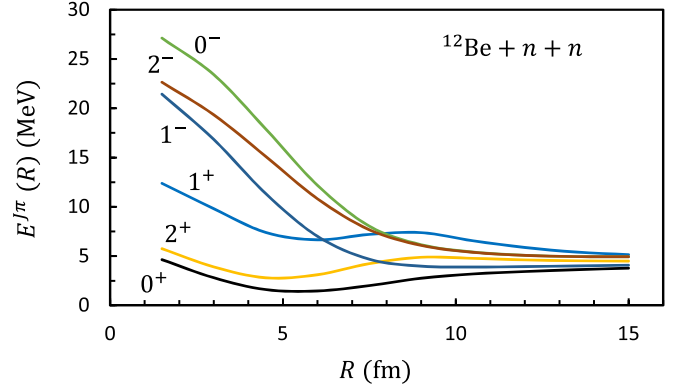


FIG. 3. $^{12}\text{Be} + n + n$ energy curves (20) for different $J\pi$ -values.

The $^{12}\text{Be} + n + n$ energy curves are displayed in Fig. 3. In positive parity, there is a minimum for $J = 0^+$ and $J = 2^+$, which correspond to the ^{14}Be ground state and to the 2^+ resonance, respectively. In negative parity, the 0^- and 2^- curves are repulsive. There is a shallow minimum for $J = 1^-$, which might be associated with a broad resonance. A deeper analysis of such resonances, however, would require a specific formalism for continuum states [8], and is beyond the scope of the present work.

An interesting characteristic of the system is provided by the energy convergence as a function of the maximum R value, which I denote as R_{\max} . In Fig. 4, I show ^{14}Be energies obtained by increasing the N value in Eq. (16) or, in other words, by increasing R_{\max} . Two different behaviors can be clearly observed. The 0^+ and 2^+ energies are almost stable above $R_{\max} \approx 10$ fm, and present a plateau. The 2^+ energy is 0.25 MeV, in nice agreement with experiment (0.28 ± 0.01 MeV [25]). This result emphasizes the importance of a microscopic theory; a non-microscopic three-body model, based on $^{12}\text{Be} + n$ and on $n + n$ phenomenological interactions, does not reproduce the 0^+ and 2^+ energies simultaneously [26]. The $^{12}\text{Be}(\text{g.s.}) + n + n$ component is 87% in the ground state, and 67% in the 2^+ resonance. This means that core excitations play a role, and may explain why nonmicroscopic models, which ignore core excitations,

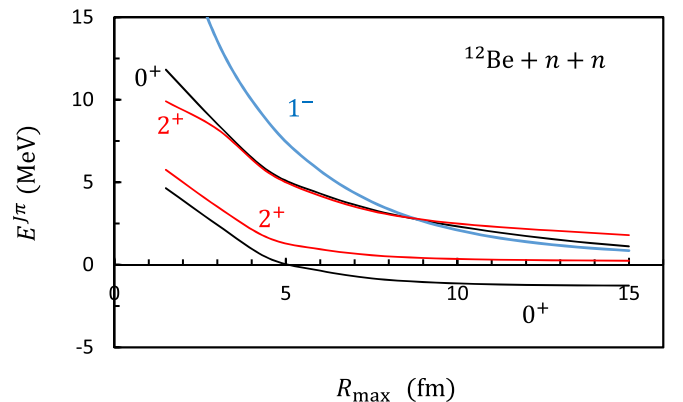


FIG. 4. Convergence of ^{14}Be energies with respect to the maximum generator coordinate R_{\max} .

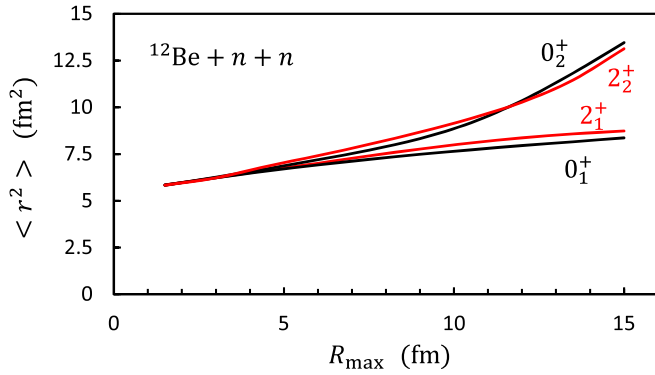


FIG. 5. Convergence of the ^{14}Be squared radius as a function of the maximum generator coordinate R_{\max} . The two first 0^+ and 2^+ eigenvalues are shown.

cannot predict the 2^+ energy accurately. The other curves in Fig. 4 do not present a plateau, which means that no further narrow resonance can be expected. In particular, the 1^- curve is typical of a continuum state where, according to the variational principle, the minimum energy is zero.

Another useful method to distinguish between narrow and broad resonances is to analyze the convergence of the r.m.s. radius $\langle r^2 \rangle$ as a function of R_{\max} . This is displayed in Fig. 5. The 0^+ and 2^+ low-lying states reach convergence near $R_{\max} \approx 12$ fm. In contrast, the second eigenvalues present a diverging behavior at large R_{\max} . This is expected since, strictly speaking, matrix elements involving continuum states diverge. Although I cannot specifically address continuum states, this technique allows a clear distinction between narrow and broad resonances. It is consistent with the energy convergence shown in Fig. 4, and confirms that r.m.s. radii in the continuum should be considered very carefully.

The ground-state radii are presented in Table I, and compared with experiment. The neutron radius is in nice agreement with experiment. The experimental proton radius, however, is significantly larger than the predicted value. This is difficult to understand from a $^{12}\text{Be} + n + n$ model, where the ^{14}Be proton radius should be close to the core proton

TABLE I. Proton, neutron and matter radii (in fm).

	$\sqrt{\langle r^2 \rangle_p}$		$\sqrt{\langle r^2 \rangle_n}$		$\sqrt{\langle r^2 \rangle_m}$	
	Th.	Exp.	Th.	Exp.	Th.	Exp.
^{14}Be	2.10	3.00(36) ^a	3.24	3.22(39) ^a	2.96	3.16(38) ^a
^{15}B	2.23	2.56(8) ^b	2.82		2.64	2.75(6) ^b
^{17}N	2.32		2.61		2.49	2.48(5) ^c
^{17}Ne	2.69	3.04(2) ^d	2.32		2.54	2.75(7) ^d
^{11}Li	1.97	2.467(37) ^e	3.12	3.36(24)	2.85	3.27(24) ^f

^aReference [27].

^bReference [28].

^cReference [29].

^dReference [30].

^eReference [31].

^fReference [32].

radius. Experimental values are partly model dependent, and a reanalysis of the ^{14}Be charge radius would be welcome.

Notice that the radii are slightly sensitive to the oscillator parameter b . From the total matter radius $\sqrt{\langle r^2 \rangle_m}$, one can define the expectation value of the hyperradius $\langle r^2 \rangle$ from

$$A\langle r_m^2 \rangle = A_1\langle r_1^2 \rangle + \langle r^2 \rangle, \quad (21)$$

where $\sqrt{\langle r_1^2 \rangle}$ is the core radius. In the shell model, this quantity is proportional to b and takes the values $\langle r_1^2 \rangle = 49b^2/24$ for ^{12}Be , $\langle r_1^2 \rangle = 27b^2/13$ for ^{13}B , $\langle r_1^2 \rangle = 32b^2/15$ for ^{15}N and ^{15}O , and $\langle r_1^2 \rangle = 17b^2/9$ for ^9Li . In contrast $\langle r^2 \rangle$, which is associated with the external neutrons, weakly depends on the oscillator parameter. For compact states, $\langle r^2 \rangle$ is small and the matter radius approximately varies linearly with b . For halo states, however, $\langle r^2 \rangle$ is the dominant term, and the matter radius is almost insensitive to the oscillator parameter.

C. ^{15}B as a $^{13}\text{B} + n + n$ system

The ^{15}B ground state is known to be bound by 3.77 MeV. Although the spin assignment is no definite, there are strong indications for a spin $J = 3/2^-$. Two excited states at $E_x = 1.336$ MeV and $E_x = 2.743$ MeV have been reported in Ref. [33]. On the theoretical side, shell-model [34] and antisymmetrized molecular dynamics (AMD, see Ref. [35]) calculations have been performed. Nonmicroscopic calculations are unavailable until now, essentially due to the lack of reliable $^{13}\text{B} + n$ potentials.

In Fig. 6, I present the energy curves of ^{15}B . As expected, the lowest energy is obtained for $J = 3/2^-$. I may also expect other bound states, corresponding to minima in the energy curves. The GCM spectrum, including all generator coordinates, is presented in Fig. 7. The theoretical spectrum shown in Fig. 7 is remarkably supported by experiment [33], although there is no spin assignment. The amount of $^{13}\text{B}(\text{g.s.}) + n + n$ component is shown for the GCM calculation. As suggested by Fig. 6, the role of core excitation is small in ^{15}B . As for ^{14}Be , the positive-parity energy curves are not completely repulsive, but do not support narrow resonances. A more reliable study of positive-parity states in ^{15}B would require introducing sd -shell components in the ^{13}B wave functions. This would considerably increase the computer times, and is not feasible at the moment.

The proton and matter radii, given in Table I are in reasonable agreement with experiment. The theoretical radius of the ^{13}B core is 2.31 fm, which means an increase of 0.33 fm for ^{15}B .

Let me briefly discuss the ^{15}Ne mirror nucleus, which has been addressed experimentally in Ref. [36] and theoretically in Ref. [37]. The ground state and first excited state have been observed in two-neutron knockout reactions from a ^{17}Ne beam at 2.5 and 4.4 MeV above the $^{13}\text{O} + p + p$ threshold. Both states are expected to be broad.

In the present model, the ^{15}B and ^{15}Ne mirror nuclei are studied in the same conditions. The energy curves are shown in Fig. 6(b). The $3/2^-$ and $5/2^-$ curves present minima, which are associated with the ground and first excited states. These minima are close to the Coulomb barrier, and clearly suggest

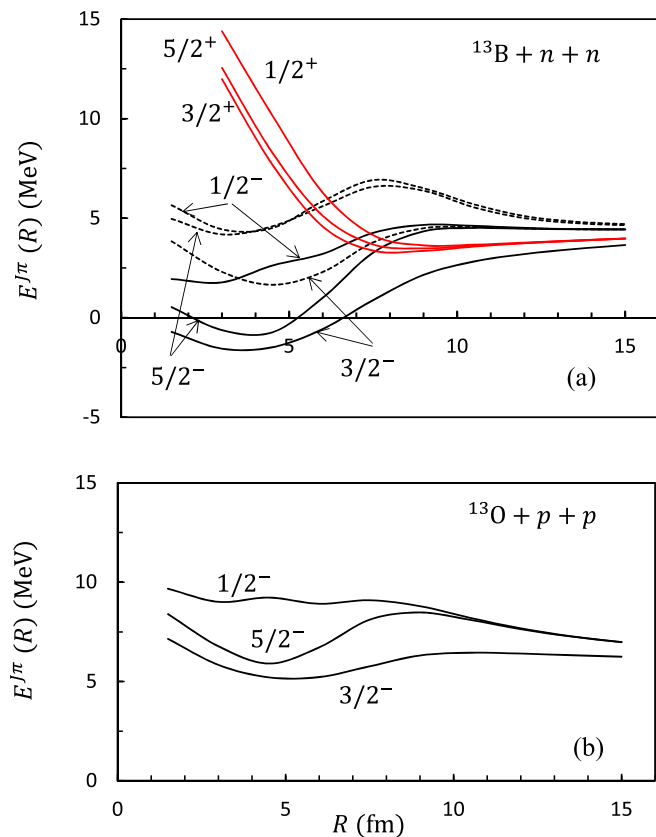


FIG. 6. (a) $^{13}\text{B} + n + n$ energy curves (20) for different $J\pi$ values. For negative parity, two eigenvalues are displayed. (b) $^{13}\text{O} + p + p$ energy curves.

continuum states. According to the higher centrifugal barrier, however, the $5/2^-$ excited state could be narrower than the $3/2^-$ ground state. The ^{15}Ne spectrum is shown in Fig. 7. Although the GCM energies are obtained in the bound-state

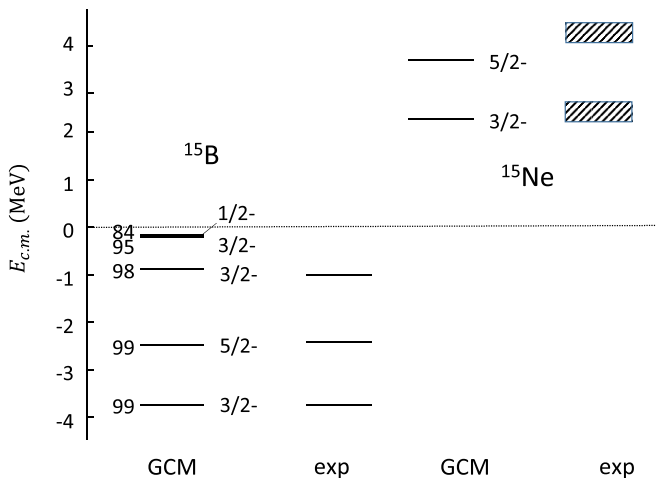


FIG. 7. ^{15}B and ^{15}Ne energy spectra, compared with experiment [33,36]. Numbers at the left of the GCM states correspond to the amount of $^{13}\text{B}(\text{g.s.}) + n + n$ configuration (in %). For ^{15}Ne , the hatched areas indicate broad resonances.

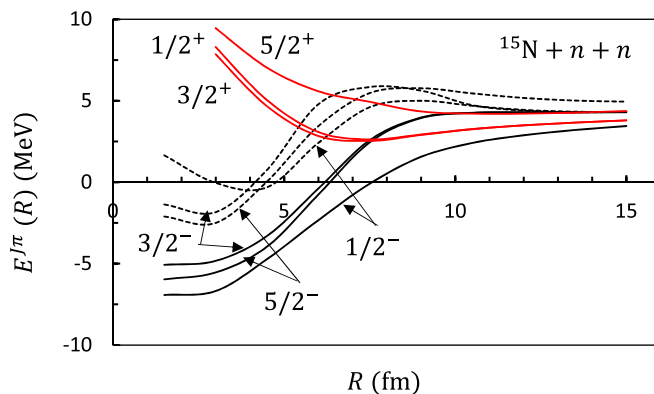


FIG. 8. $^{15}\text{N} + n + n$ energy curves (20) for different $J\pi$ values.

approximation, the results are close to the energies observed experimentally [36].

D. ^{17}N as $^{15}\text{N} + n + n$ and ^{17}Ne as $^{15}\text{O} + p + p$ systems

Microscopic calculations involving a ^{15}N or a ^{15}O core are relatively simple since only the ground state $1/2^-$ and the first excited state $3/2^-$ are present in the $0\hbar\omega$ shell model. A previous three-cluster microscopic calculation was performed in Ref. [38], where the main goal was to address the possible existence of a proton halo in ^{17}Ne . Figure 8 shows the energy curves, which present a minimum near $R = 0$ for negative-parity. This suggests a compact structure for negative-parity states, in contrast with the other systems considered here.

The ^{17}N spectrum is displayed in Fig. 9. The general agreement with experiment is reasonable but, as in Ref. [38] the ordering of the two first excited states is incorrect. For all states the $^{15}\text{N}(\text{g.s.}) + n + n$ component is dominant. No

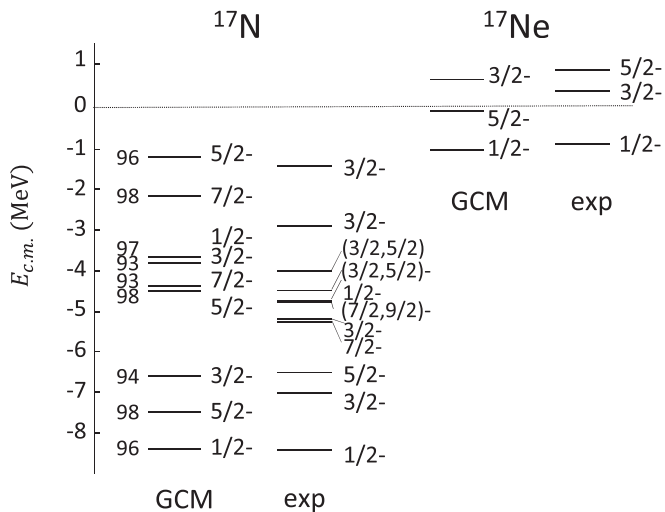


FIG. 9. ^{17}N and ^{17}Ne energy spectra, compared with experiment [44]. Only negative-parity states are shown. Numbers at the left of GCM states correspond to the amount of $^{15}\text{N}(\text{g.s.}) + n + n$ configuration (in %).

TABLE II. $E2$ electromagnetic transition probabilities (in $e^2\text{fm}^4$) in ^{17}Ne . No effective charge is used.

	GCM	Exp.
$1/2^- \rightarrow 5/2^-$	92.9	90 ± 18 [43], 124 ± 18 [42]
$1/2^- \rightarrow 3/2^-$	68.0	68^{+19}_{-25} [41]
$5/2^- \rightarrow 3/2^-$	7.1	

positive parity state is found, as suggested by the repulsive energy curves of Fig. 8.

The ^{17}Ne spectrum is studied with the same nucleon-nucleon interaction; the Majorana parameter is the same as in ^{17}N . The GCM reproduces the binding energy very well (-1.05 MeV in the model, to be compared to the experimental value -0.93 MeV), which shows that the Coulomb shift is accurately described.

Electromagnetic transitions have been suggested to be a valuable tool to investigate the structure of ^{17}Ne [39,40]. The $E2$ transition probabilities have been studied by relativistic Coulomb excitation with a ^{17}Ne radioactive beam [41–43]. The $B(E2)$ values, computed without any effective charge, are presented in Table II. The $B(E2, 1/2^- \rightarrow 5/2^-)$ GCM value is in excellent agreement with the latest data of Marganec *et al.* [43]. The experimental value of Chromik *et al.* [42] is larger, but is probably influenced by nuclear effects, which have been dismissed in the analysis [43]. The transition to the $3/2^-$ state is also well reproduced, which shows that the GCM wave functions are reliable.

The matter radius of the ^{17}N ground state, given in Table I, is in excellent agreement with experiment [29]. For ^{17}Ne , however, even if the binding energy is lower, the GCM does not support the large difference with ^{17}N . I rather confirm the conclusion of Ref. [38], that there is no evidence for a proton halo in ^{17}Ne .

E. ^{11}Li as a $^9\text{Li} + n + n$ system

The ^{11}Li nucleus has been studied in many experimental and theoretical works. The very low binding energy ($S_{2n} = 0.367$ MeV [24]) is responsible for a remarkable halo structure, as suggested by the large r.m.s. radius. The present calculation is made difficult because of the large number of Slater determinants (90) involved in the ^9Li core. A previous microscopic three-cluster study was performed in Ref. [45], but with a frozen triangular geometry. In Ref. [46], the authors describe the core in an $\alpha + t + n + n$ multicluster configuration.

The $^9\text{Li} + n + n$ energy curves are displayed in Fig. 10. A minimum is obtained for $J = 3/2^-$ and, to a lesser extent, for $J = 1/2^-$. The $3/2^-$ minimum corresponds to the ^{11}Li ground state. The role of core excitations is illustrated in Fig. 2. When core excitations are neglected, the state is unbound. The importance of core excitations was already pointed out in Ref. [46]. In contrast with the previous examples, where the neutron number of the core $N = 8$ corresponds to a closed shell, the various $^9\text{Li} + n + n$ configurations are not orthogonal to each other. Consequently, a ground-state component in ^{11}Li cannot be estimated.

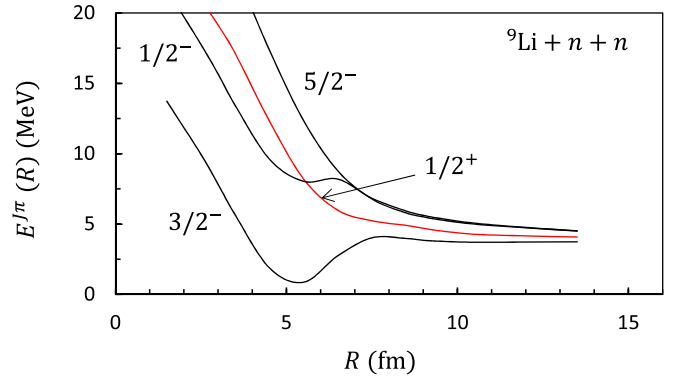


FIG. 10. $^9\text{Li} + n + n$ energy curves (20) for different $J\pi$ values.

The proton, neutron and matter radii are presented in Table I. The calculation confirms the large enhancement of the matter radius, compared to the ^9Li core [the shell-model value is $\sqrt{\langle r^2 \rangle_m(^9\text{Li})} = b\sqrt{17/9} = 2.20$ fm]. The GCM value is, however, slightly smaller than experiment. For the proton radius, the experimental ^{11}Li value (2.467 fm) is significantly larger than the ^9Li value (2.217 fm), which suggests that the neutron halo of ^{11}Li affects the core [31,47]. In the present model, the ^9Li proton radius is $\sqrt{\langle r^2 \rangle_p(^9\text{Li})} = b\sqrt{4/3} = 1.84$ fm. The difference between ^{11}Li and ^9Li is therefore 0.13 fm, which is smaller than experiment (0.25 fm) (see a detailed discussion in Refs. [31,47]).

IV. CONCLUSION

The main goal of the present work is to extend the hyperspherical formalism to microscopic three-cluster models. The hyperradial functions are expanded over a Gaussian basis using the generator coordinate method. Then the wave functions are expressed in terms of projected Slater determinants. This approach is well adapted to multicluster systems. With a single generator coordinate, it provides an accurate description of the wave functions, even at long distances. The calculations of the matrix elements, however, require very long computer times, owing to the seven-dimension integrals necessary for the angular momentum projection. The extension to p -shell cores raises additional difficulties due to (i) the quadruple sums involved in the matrix elements of two-body interactions; (ii) the presence of several Slater determinants; (iii) the introduction of core excited states. The calculations are made possible thanks to an efficient parallelization of the computer code.

The model has been applied to some exotic light nuclei: ^{14}Be , ^{15}B , ^{17}Ne , and ^{11}Li . In all cases, the only parameter (the admixture parameter M involved in the Volkov nucleon-nucleon interaction) is adjusted on the ground-state energy. For ^{14}Be , the 2^+ excitation energy is well reproduced, in contrast with nonmicroscopic models. The GCM spectrum of ^{15}B is in nice agreement with the experimental energies. An exploratory study of the ^{15}Ne mirror system, which is unbound, is consistent with the experimental energies, and suggests that the first excited state is narrower than the ground state. The ^{17}N spectrum presents many states, which, in

general, are fairly well reproduced by the GCM. The ground state is confirmed to be $1/2^-$, but the order of the first two excited states is incorrect, as in Ref. [38]. In the ^{17}Ne mirror nucleus, the ground-state energy, as well as $E2$ transition probabilities are in good agreement with experiment. For ^{11}Li , calculations are extremely long, owing to the 90 Slater determinants involved in the core. The neutron and matter radii are explained fairly well, but the proton radius is smaller than the experimental value.

The present model could be extended to deal with three-body continuum states [8]. On the other hand, the wave functions could be used as an input to determine scattering cross sections, as it was done for ^6He for example [9].

ACKNOWLEDGMENTS

P. D. is Directeur de Recherches of F.R.S.-FNRS, Belgium. This work was supported by the Fonds de la Recherche Scientifique - FNRS under Grant No. 4.45.10.08. It benefited from computational resources made available on the Tier-1 super-computer of the Fédération Wallonie-Bruxelles, infrastructure funded by the Walloon Region under the Grant Agreement No. 1117545.

APPENDIX: CORE WAVE FUNCTIONS

In this Appendix I give some detail about the core wave functions (5). The quantum numbers (I, L, S, T) are given in Table III. First, the list of functions $\bar{\Phi}_i$ is determined, and is then used to diagonalize the operators I^2, L^2, S^2 , and T^2 . The diagonalization provides eigenvalues and coefficients d_i^{lvLST} , which do not depend on the Hamiltonian.

TABLE III. Quantum numbers (I, L, S, T) of the core wave functions. n is the degeneracy.

	I	T	S	L	n		
^9Li	1/2	3/2	1/2	0	1		
				1	2		
			3/2	3/2	3/2	1	1
					2	2	
	3/2	3/2	1/2	1	1		
				1	2		
			3/2	1/2	1/2	1	2
					0	1	
			5/2	3/2	1/2	1	1
						2	1
	^{12}Be	7/2	3/2	1/2	3	1	
					3/2	2	1
		0	2	0	0	1	
					1	1	
1		2	1	1	1		
				2	1		
2		2	0	2	1		
				2	1		
^{13}B		1/2	3/2	1/2	1	1	
					1	1	
	3/2	3/2	1/2	1	1		
				2	1		
	5/2	3/2	1/2	2	1		
				0	1		
^{15}N	1/2	1/2	1/2	1	1		
				1	1		
	3/2	1/2	1/2	1	1		
				1	1		

- [1] I. Tanihata, H. Savajols, and R. Kanungo, *Prog. Part. Nucl. Phys.* **68**, 215 (2013).
- [2] C. D. Lin, *Phys. Rep.* **257**, 1 (1995).
- [3] M. Gattobigio, A. Kievsky, and M. Viviani, *Phys. Rev. C* **83**, 024001 (2011).
- [4] P. Descouvemont and M. Dufour, in *Clusters in Nuclei*, edited by C. Beck, Vol. 2 (Springer, Berlin, 2012).
- [5] H. Horiuchi, K. Ikeda, and K. Katō, *Prog. Theor. Phys. Suppl.* **192**, 1 (2012).
- [6] G. F. Filippov, K. Katō, and S. V. Korennov, *Prog. Theor. Phys.* **96**, 575 (1996).
- [7] S. Korennov and P. Descouvemont, *Nucl. Phys. A* **740**, 249 (2004).
- [8] A. Damman and P. Descouvemont, *Phys. Rev. C* **80**, 044310 (2009).
- [9] P. Descouvemont, *Phys. Rev. C* **93**, 034616 (2016).
- [10] P. Descouvemont and E. C. Pinilla, *Few-Body Systems* **60**, 11 (2019).
- [11] Y. Blumenfeld, T. Nilsson, and P. Van Duppen, *Phys. Scr.* **T152**, 014023 (2013).
- [12] K. Wildermuth and Y. C. Tang, in *A Unified Theory of the Nucleus*, edited by K. Wildermuth and P. Kramer (Vieweg, Braunschweig, 1977).
- [13] A. B. Volkov, *Nucl. Phys.* **74**, 33 (1965).
- [14] D. R. Thompson, M. LeMere, and Y. C. Tang, *Nucl. Phys. A* **286**, 53 (1977).
- [15] R. Machleidt, Q. MacPherson, E. Marji, R. Winzer, C. Zeoli, and D. R. Entem, *Few-Body Systems* **54**, 821 (2013).
- [16] Y. Kanada-En'yo and Y. Akaishi, *Phys. Rev. C* **69**, 034306 (2004).
- [17] N. Itagaki, *Phys. Rev. C* **94**, 064324 (2016).
- [18] H. Horiuchi, *Prog. Theor. Phys. Suppl.* **62**, 90 (1977).
- [19] P. Descouvemont, *Nucl. Phys. A* **584**, 532 (1995).
- [20] P. Descouvemont, *Phys. Rev. C* **70**, 065802 (2004).
- [21] M. V. Zhukov, B. V. Danilin, D. V. Fedorov, J. M. Bang, I. J. Thompson, and J. S. Vaagen, *Phys. Rep.* **231**, 151 (1993).
- [22] A. Kievsky, S. Rosati, M. Viviani, L. E. Marcucci, and L. Girlanda, *J. Phys. G* **35**, 063101 (2008).
- [23] P. Descouvemont and D. Baye, *Nucl. Phys. A* **573**, 28 (1994).
- [24] G. Audi, F. G. Kondev, M. Wang, W. Huang, and S. Naimi, *Chin. Phys. C* **41**, 030001 (2017).
- [25] T. Sugimoto, T. Nakamura, Y. Kondo, N. Aoi, H. Baba, D. Bazin, N. Fukuda, T. Gomi, H. Hasegawa, N. Imai, M. Ishihara, T. Kobayashi, T. Kubo, M. Miura, T. Motobayashi, H. Otsu, A. Saito, H. Sakurai, S. Shimoura, A. Vinodkumar, K. Watanabe,

- Y. Watanabe, T. Yakushiji, Y. Yanagisawa, and K. Yoneda, *Phys. Lett. B* **654**, 160 (2007).
- [26] P. Descouvemont, E. M. Tursunov, and D. Baye, *Nucl. Phys. A* **765**, 370 (2006).
- [27] I. Tanihata, T. Kobayashi, O. Yamakawa, S. Shimoura, K. Ekuni, K. Sugimoto, N. Takahashi, T. Shimoda, and H. Sato, *Phys. Lett. B* **206**, 592 (1988).
- [28] A. Estradé, R. Kanungo, W. Horiuchi, F. Ameil, J. Atkinson, Y. Ayyad, D. Cortina-Gil, I. Dillmann, A. Evdokimov, F. Farinon, H. Geissel, G. Guastalla, R. Janik, M. Kimura, R. Knöbel, J. Kurcewicz, Y. A. Litvinov, M. Marta, M. Mostazo, I. Mukha, C. Nociforo, H. J. Ong, S. Pietri, A. Prochazka, C. Scheidenberger, B. Sitar, P. Strmen, Y. Suzuki, M. Takechi, J. Tanaka, I. Tanihata, S. Terashima, J. Vargas, H. Weick, and J. S. Winfield, *Phys. Rev. Lett.* **113**, 132501 (2014).
- [29] A. Ozawa, T. Kobayashi, H. Sato, D. Hirata, I. Tanihata, O. Yamakawa, K. Omata, K. Sugimoto, D. Olson, W. Christie, and H. Wieman, *Phys. Lett. B* **334**, 18 (1994).
- [30] W. Geithner, T. Neff, G. Audi, K. Blaum, P. Delahaye, H. Feldmeier, S. George, C. Guénaut, F. Herfurth, A. Herlert, S. Kappertz, M. Keim, A. Kellerbauer, H.-J. Kluge, M. Kowalska, P. Lievens, D. Lunney, K. Marinova, R. Neugart, L. Schweikhard, S. Wilbert, and C. Yazidjian, *Phys. Rev. Lett.* **101**, 252502 (2008).
- [31] R. Sánchez, W. Nörtershäuser, G. Ewald, D. Albers, J. Behr, P. Bricault, B. A. Bushaw, A. Dax, J. Dilling, M. Dombisky, G. W. F. Drake, S. Götze, R. Kirchner, H.-J. Kluge, T. Kühl, J. Lassen, C. D. P. Levy, M. R. Pearson, E. J. Prime, V. Ryjkov, A. Wojtaszek, Z.-C. Yan, and C. Zimmermann, *Phys. Rev. Lett.* **96**, 033002 (2006).
- [32] I. Tanihata, H. Hamagaki, O. Hashimoto, Y. Shida, N. Yoshikawa, K. Sugimoto, O. Yamakawa, T. Kobayashi, and N. Takahashi, *Phys. Rev. Lett.* **55**, 2676 (1985).
- [33] R. Kanungo, Z. Elekes, H. Baba, Z. Dombrádi, Z. Fülöp, J. Gibelin, Á. Horváth, Y. Ichikawa, E. Ideguchi, N. Iwasa, H. Iwasaki, S. Kawai, Y. Kondo, T. Motobayashi, M. Notani, T. Ohnishi, A. Ozawa, H. Sakurai, S. Shimoura, E. Takeshita, S. Takeuchi, I. Tanihata, Y. Togano, C. Wu, Y. Yamaguchi, Y. Yanagisawa, A. Yoshida, and K. Yoshida, *Phys. Lett. B* **608**, 206 (2005).
- [34] E. K. Warburton and B. A. Brown, *Phys. Rev. C* **46**, 923 (1992).
- [35] Y. Kanada-En'yo and H. Horiuchi, *Phys. Rev. C* **52**, 647 (1995).
- [36] F. Wamers, J. Marganec, F. Aksouh, Y. Aksyutina, H. Álvarez-Pol, T. Aumann, S. Beceiro-Novo, K. Boretzky, M. J. G. Borge, M. Chartier, A. Chatillon, L. V. Chulkov, D. Cortina-Gil, H. Emling, O. Ershova, L. M. Fraile, H. O. U. Fynbo, D. Galaviz, H. Geissel, M. Heil, D. H. H. Hoffmann, H. T. Johansson, B. Jonson, C. Karagiannis, O. A. Kiselev, J. V. Kratz, R. Kulesa, N. Kurz, C. Langer, M. Lantz, T. Le Bleis, R. Lemmon, Y. A. Litvinov, K. Mahata, C. Müntz, T. Nilsson, C. Nociforo, G. Nyman, W. Ott, V. Panin, S. Paschalis, A. Perea, R. Plag, R. Reifarth, A. Richter, C. Rodríguez-Tajes, D. Rossi, K. Riisager, D. Savran, G. Schrieder, H. Simon, J. Stroth, K. Sümmerner, O. Tengblad, H. Weick, C. Wimmer, and M. V. Zhukov, *Phys. Rev. Lett.* **112**, 132502 (2014).
- [37] T. Golubkova, X.-D. Xu, L. Grigorenko, I. Mukha, C. Scheidenberger, and M. Zhukov, *Phys. Lett. B* **762**, 263 (2016).
- [38] N. Timofeyuk, P. Descouvemont, and D. Baye, *Nucl. Phys. A* **600**, 1 (1996).
- [39] L. V. Grigorenko, Y. L. Parfenova, and M. V. Zhukov, *Phys. Rev. C* **71**, 051604(R) (2005).
- [40] H. T. Fortune, *Phys. Rev. C* **97**, 014308 (2018).
- [41] M. J. Chromik, B. A. Brown, M. Fauerbach, T. Glasmacher, R. Ibbotson, H. Scheit, M. Thoennessen, and P. G. Thirolf, *Phys. Rev. C* **55**, 1676 (1997).
- [42] M. J. Chromik, P. G. Thirolf, M. Thoennessen, B. A. Brown, T. Davinson, D. Gassmann, P. Heckman, J. Prisciandaro, P. Reiter, E. Tryggestad, and P. J. Woods, *Phys. Rev. C* **66**, 024313 (2002).
- [43] J. Marganec, F. Wamers, F. Aksouh, Y. Aksyutina, H. Álvarez-Pol, T. Aumann, S. Beceiro-Novo, C. Bertulani, K. Boretzky, M. Borge, M. Chartier, A. Chatillon, L. Chulkov, D. Cortina-Gil, H. Emling, O. Ershova, L. Fraile, H. Fynbo, D. Galaviz, H. Geissel, M. Heil, D. Hoffmann, J. Hoffmann, H. Johansson, B. Jonson, C. Karagiannis, O. Kiselev, J. Kratz, R. Kulesa, N. Kurz, C. Langer, M. Lantz, T. L. Bleis, R. Lemmon, Y. Litvinov, K. Mahata, C. Müntz, T. Nilsson, C. Nociforo, G. Nyman, W. Ott, V. Panin, S. Paschalis, A. Perea, R. Plag, R. Reifarth, A. Richter, C. Rodríguez-Tajes, D. Rossi, K. Riisager, D. Savran, G. Schrieder, H. Simon, J. Stroth, K. Sümmerner, O. Tengblad, S. Typel, H. Weick, M. Wiescher, and C. Wimmer, *Phys. Lett. B* **759**, 200 (2016).
- [44] D. R. Tilley, H. R. Weller, and C. M. Cheves, *Nucl. Phys. A* **564**, 1 (1993).
- [45] P. Descouvemont, *Nucl. Phys. A* **626**, 647 (1997).
- [46] K. Varga, Y. Suzuki, and R. G. Lovas, *Phys. Rev. C* **66**, 041302(R) (2002).
- [47] M. Puchalski, A. M. Moro, and K. Pachucki, *Phys. Rev. Lett.* **97**, 133001 (2006).